


# Fabrication of Functionally Graded Ti and $\gamma$ -TiAl by Laser Metal Deposition

LEI YAN <sup>1,3,4</sup> XUEYANG CHEN,<sup>1</sup> YUNLU ZHANG,<sup>1</sup>  
JOSEPH W. NEWKIRK,<sup>2</sup> and FRANK LIOU<sup>1</sup>

1.—Department of Mechanical and Aerospace Engineering, Missouri University of Science and Technology, Rolla, MO, USA. 2.—Department of Materials Science and Engineering, Missouri University of Science and Technology, Rolla, MO, USA. 3.—e-mail: lyvh8@mst.edu. 4.—e-mail: lei.aaron.yan@gmail.com

TiAl alloys have become a popular choice in the aerospace and automotive industries, owing to their high specific yield strength, specific modulus, and oxidation resistance over titanium alloys and Ni-based super alloys at elevated temperatures. Although laser metal deposition (LMD) techniques have been available for manufacturing metal alloys for a decade, limited research has been focused on joining intermetallic materials with dissimilar materials using LMD. Here, LMD was used to join titanium aluminide Ti-48Al-2Cr-2Nb and commercially pure titanium with an innovative transition path. The theorized transition was implemented by fabricating functionally graded material (FGM). Porosity- and crack-free deposits were successfully fabricated. Energy dispersive x-ray spectroscopy analysis revealed the final composition was very close to the design composition. X-ray diffraction showed the expected phases were formed. The Vickers hardness, ultimate tensile strength, and coefficient of thermal expansion were evaluated to characterize the FGM's mechanical and physical properties. The properties of the material were comparable to those of as-cast material as reported in the literature.

## INTRODUCTION

TiAl alloys are currently considered excellent candidates for replacing nickel-based and titanium (Ti) alloys in automotive and aerospace applications because of their low density, high temperature strength, high stiffness, and good corrosion and oxidation resistance.<sup>1,2</sup> Up to now, the GEnX jet engine equipped with cast TiAl blades has been regarded as the most successful commercial application in TiAl technology.<sup>3</sup> TiAl alloy's inherent brittleness is susceptible to solid-state cracking, which causes difficulty in conventional manufacturing techniques.<sup>4,5</sup> To address those issues, laser metal deposition (LMD) was introduced as a potential solution because of its advantages of suppressing solid-state transformations, refining microstructural features, and reducing segregation.<sup>6,7</sup> Parts with different TiAl alloys have been successfully fabricated with the LMD method;<sup>8–10</sup> however, additional experiment set-up, such as insulation and inductive heating, is still required

to control the heat flow during the deposition process to solve the fast cooling-caused cracking issue, restricting the feasibility of the LMD process.<sup>11,12</sup> Functionally graded material (FGM) was theorized in the early 1970s and offers the possibility of joining dissimilar materials with gradient compositional changes in between, which helps to increase the final part of the mechanical performance.<sup>13</sup> LMD is increasingly suitable for FGM part fabrication, especially when coupled with pre-mixed powders or multi-nozzles, and the success in developing Ti-6Al-4V to SS316<sup>14</sup> and 304L to Invar 36<sup>15</sup> has shown the incomparable advantages of LMD and FGM over conventional methods. The challenge of FGM is the gradient composition and laser energy input selection along the gradient path.<sup>14,15</sup> The intent of this article is to provide a new method to fabricate Ti/TiAl FGM, which is a new candidate material for aero-engine turbine blades and turbine discs, without extra heat flow control equipment. Ti-48Al is found to have the maximum room temperature ductility in binary TiAl alloys, and Cr and Nb

additions are made for room temperature ductility and oxidation resistance improvement.<sup>16</sup> Herein, Ti/Ti-48Al-2Cr-2Nb (Ti/Ti4822) gradient material was successfully fabricated by the LMD process. Chemical and phase compositions across the as-deposited specimen were investigated. The Vickers hardness and tensile property along the build direction was evaluated. The coefficient of thermal expansion (CTE) was also measured at temperatures ranging from 23.9°C to 509.4°C.

## MATERIALS AND METHODS

TiAl alloys with potential practical use are based on a dual-phase ( $\alpha_2 + \gamma$ ) microstructure, which has an aluminum content between 37% and 49% (at.%).<sup>17</sup> From quaternary Ti-Al-Cr-Nb system phase diagrams,<sup>18,19</sup>  $\alpha$ ,  $\alpha_2$ , and  $\gamma$  are found to be the three main phases present with an aluminum content below 60% and Nb and Cr less than 2% (at.%). According to the above analysis, a transition path containing six regions with a gradient changing wt.% of Ti and Ti4822 was used to join the CP grade 2 Ti plate and Ti4822. Figure 1a presents the details of the powder blend composition and possible phases in each region. Gas atomized powders were used, where Ti4822 powder containing 34.4 Al, 2.38 Cr, 4.75 Nb, 0.128 O, 0.04 Fe and balanced Ti, Ti powder containing 0.12 Fe, 0.16 O, and 0.01 C and balanced Ti (all composition in wt.%). The Ti4822 powder particle size distribution follows  $D_{10}$  59  $\mu\text{m}$ ,  $D_{50}$  94  $\mu\text{m}$ , and  $D_{90}$  137  $\mu\text{m}$ . Ti powder represents a similar particle size distribution as Ti4822,  $D_{10}$  66  $\mu\text{m}$ ,  $D_{50}$  105  $\mu\text{m}$ , and  $D_{90}$  141  $\mu\text{m}$ .

In the current work, gradient thin-wall samples were built using a side nozzle LMD system with a 1-kW solid-state YAG-fiber laser, 3-axis numerical control work table, and argon as inert atmosphere gas; the schematic of the experimental set-up is shown in Fig. 1b.<sup>16</sup> During LMD processing, the total incident energy input is critically important and defined as  $P/v$ , where  $P$  is the laser power, and  $v$  is laser scan speed.<sup>7,12</sup> The incident energy input was continuously optimized to avoid poor melting and overheating, which lead directly to severe burning and cracks.<sup>7</sup> The final utilized incident energy input is presented in Table I.

In regions 1, 2, and 3, the high-energy input at the beginning of deposition was used to create the molten pool and then decreased later to avoid overheating. In regions 4, 5, and 6, less energy input was applied because of heat accumulating in the structure as the build height increased. One-dimensional heat flow in the thin-wall structure causes a slow heat transfer from the deposit to substrate.<sup>20</sup> The Nb and Cr content increase in the powder blends also led to less energy being required in the deposition process.<sup>21,22</sup> Here, the laser scan speed was set to 600 mm/min with varied laser power to control the input energy. Each region consists of 50 layers of 0.1-mm-thick single track. The final gradient part was then electrical discharge machining (EDM) sectioned, mounted, and polished according to the standard metallographic procedure. The polished sample was etched using a 100 mL  $\text{HNO}_3$ , 100 mL HF, and 300 mL  $\text{H}_2\text{O}$  solution.

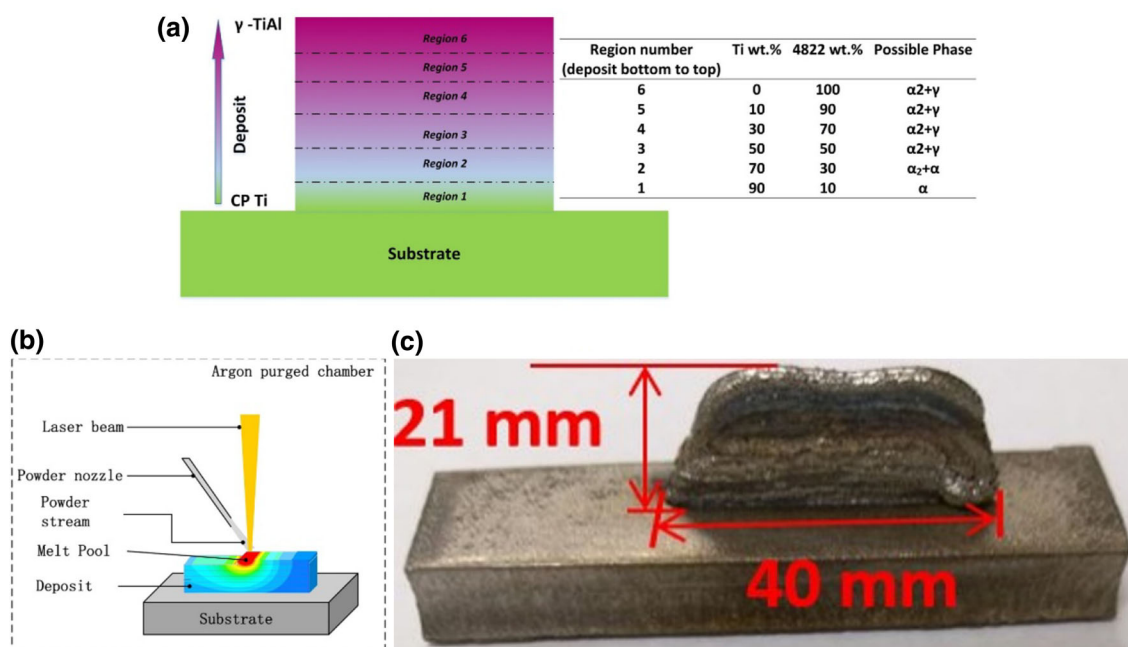


Fig. 1. Ti/Ti4822 FGM build plan and final product, (a) a gradient transition path to join Ti and Ti4822 with the predicted phase composition, (b) schematic of the LMD system, and (c)  $\gamma$ -TiAl FGM deposit.

**Table I. Run log of incident energy applied in different regions**

<u>Region number</u>	<u>Layer number</u>	<u>Incident energy (<math>\text{Jmm}^{-1}</math>)</u>
Region 1	1–3	82
	4–7	70
	8–50	60
Region 2	1–2	82
	3–6	70
	7–16	60
	17–50	40
Region 3	1–2	82
	3–6	70
	7–12	60
	13–50	40
Region 4	1–10	60
	11–50	40
Region 5	1–2	60
	3–50	40
Region 6	1–50	40

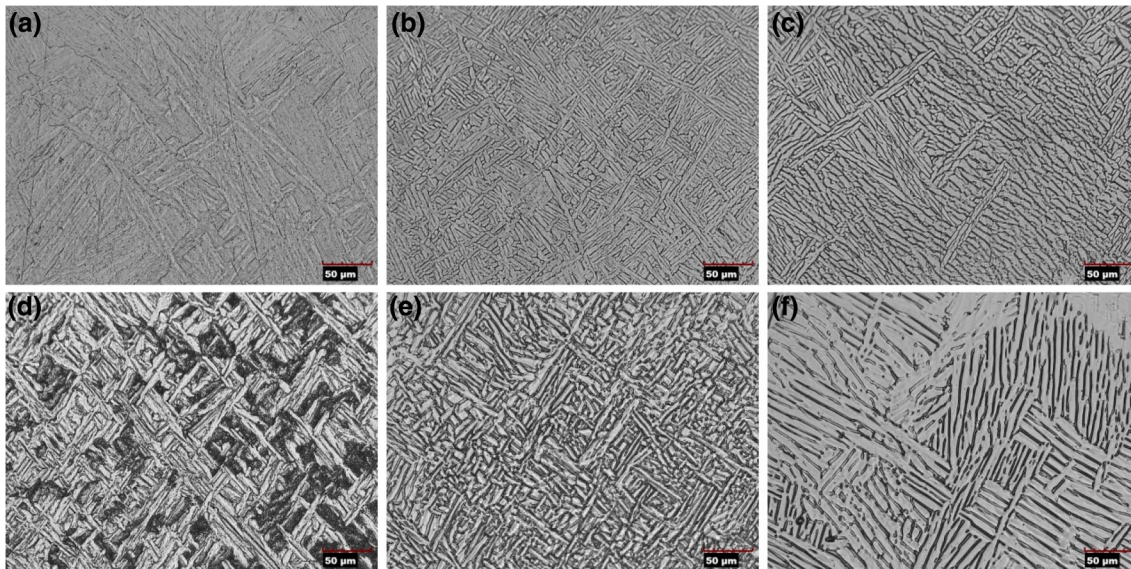


Fig. 2. Microstructure across the gradient alloy, (a) region 1, (b) region 2, (c) region 3, (d) region 4, (e) region 5, and (f) region 6.

## RESULTS AND DISCUSSIONS

The final FGM deposit has dimensions of  $40 \text{ mm} \times 2.2 \text{ mm} \times 21 \text{ mm}$  as shown in Fig. 1c, and no porosity was found across the etched gradient part by scanning electron microscope (SEM). The typical microstructure in six regions is presented in Fig. 2, which shows the major form of the microstructure in regions 1–5 is basketweave and in region 6 is lamellar. In the thin-wall structure, the cooling rate decreases as the deposit height increases,<sup>12</sup> and the higher cooling rate benefits the basketweave formation.<sup>2</sup> Due to the cooling rate increase from top to bottom in the deposit, region 6–1 tends to have a finer lath, which results in a higher UTS value.

The XRD pattern was obtained across the whole gradient section, and the existence of three as-planned phases was further confirmed. The results, shown Fig. 3a, reveal strong peaks of  $\alpha$ ,  $\alpha_2$ , and  $\gamma$  phase, which denote a high concentration of those phases in the final part.

EDS line scan was utilized to characterize the chemical composition distribution along the transition path. The substrate and six regions are clearly revealed as shown in Fig. 3b (only elements Ti and Al are demonstrated). On the substrate, at.% of Ti increased from 90 to 100, while Al decreased from 10 to zero within a  $1000\text{-}\mu\text{m}$  dilution zone. From region 1–6, each region has a status with almost constant at.% of Ti and Al and transitions into

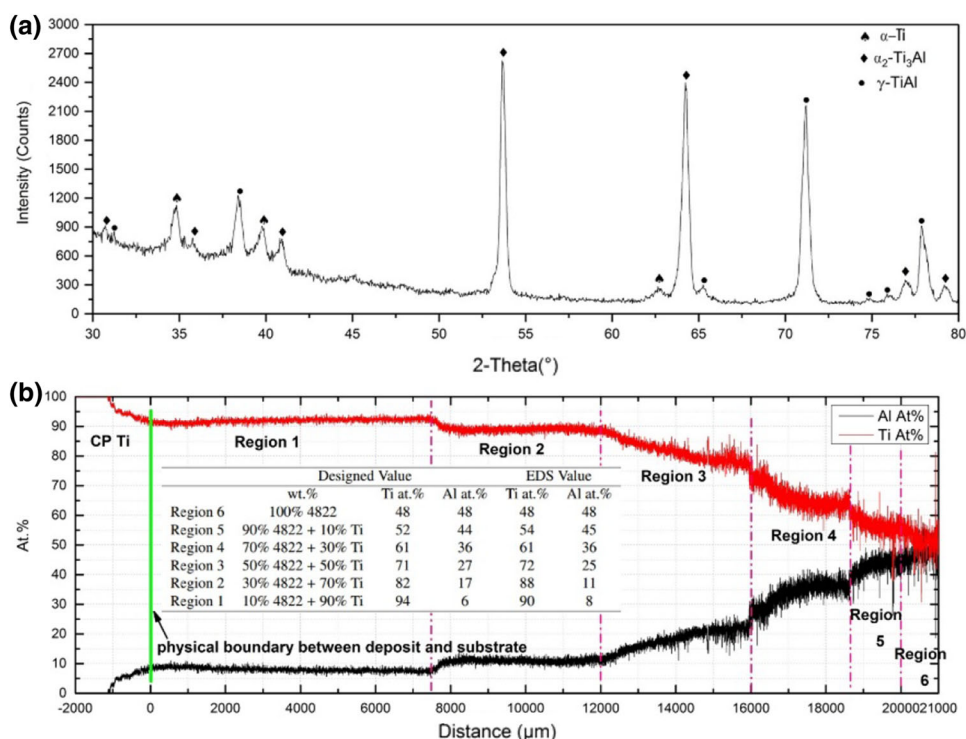


Fig. 3. Chemical composition and phase analysis across the gradient alloy, (a) XRD pattern of the Ti/Ti4822 gradient alloy and (b) EDS line scan results.

neighboring regions through about 50- $\mu$ m-wide diffusion zones. In each region, the measured at.% of Ti and Al is close to the designed ones as shown in the inset table of Fig. 3b, which comes from a similar particle size and density of Ti and TiAl powder in the powder blends and makes those two kinds of powder have a similar possibility be introduced into the molten pool.<sup>23,24</sup> An as-deposited and designed region height difference resulted from the drawbacks of the one-hopper side nozzle system where minor misalignment of the laser and nozzle during powder changes for different region fabrications can lead to less powder being introduced into the molten pool and reflects as the region height difference.<sup>25,26</sup> But those height differences also show the possibility to join CP Ti and Ti4822 with a shorter transition path. A coaxial nozzle system with mass flow controllability for each hopper would be a better option for FGM part fabrication.

Vickers hardness along the gradient path as shown in Fig. 4a exhibits a stabilized value of  $372 \pm 15$  HV1 throughout 0–14,000  $\mu$ m high, where region 1, region 2, and the lower half of region 3 belong. Then, there is a slight increase of the hardness from 14,000  $\mu$ m to the monolithic Ti4822 region, where the average value is  $435 \pm 15$  HV1. According to the Vickers hardness distribution, the hardness increased as the Ti4822 wt.% increased, and the maximum hardness value 465 HV1 was at the interface of region 5 and 6. The mean hardness

at the dilution zone of region 1 and the substrate dropped from 350 HV1 to 170 HV1, and the hardness difference is attributed to the formation of the nearly lamellar fine structures.<sup>27</sup>

To evaluate tensile strength at different heights along the laser scan direction within the gradient alloy, the specimen was EDM cut, as shown in Fig. 4c, into the dimensions given in Fig. 4b. The specimen was polished to remove defects and pulled on Instron<sup>®</sup> 5966 at a test speed of 0.1 mm/min. Figure 4d shows in region 1 the UTS value is 800–1100 MPa and decreases to 200–400 MPa in region 2 to region 6, which correlates to the Ti4822 wt.% increase causing the UTS decrease. The monolithic Ti4822 region shows UTS at 380 MPa and the elongation less than 1%, which has a comparable value to as-cast  $\gamma$ -TiAl.<sup>28</sup>

The digital image correlation (DIC) method was used to characterize the CTE property along the build direction within the gradient alloy.<sup>29</sup> The as-deposited part was EDM cut into a 27.5 mm  $\times$  5 mm  $\times$  1-mm piece across the substrate to region 6 and tested with the experimental set-up demonstrated in Fig. 4e, where a hot plate is used to heat up the specimen and a camera is used to take a video that covers the whole heating and cooling process. Four K-type thermal couples were implemented to record the temperature history during the CTE testing. Seven color regions could be identified from left to right in Fig. 4f, which is from Ti4822 to CP Ti. The average CTE values

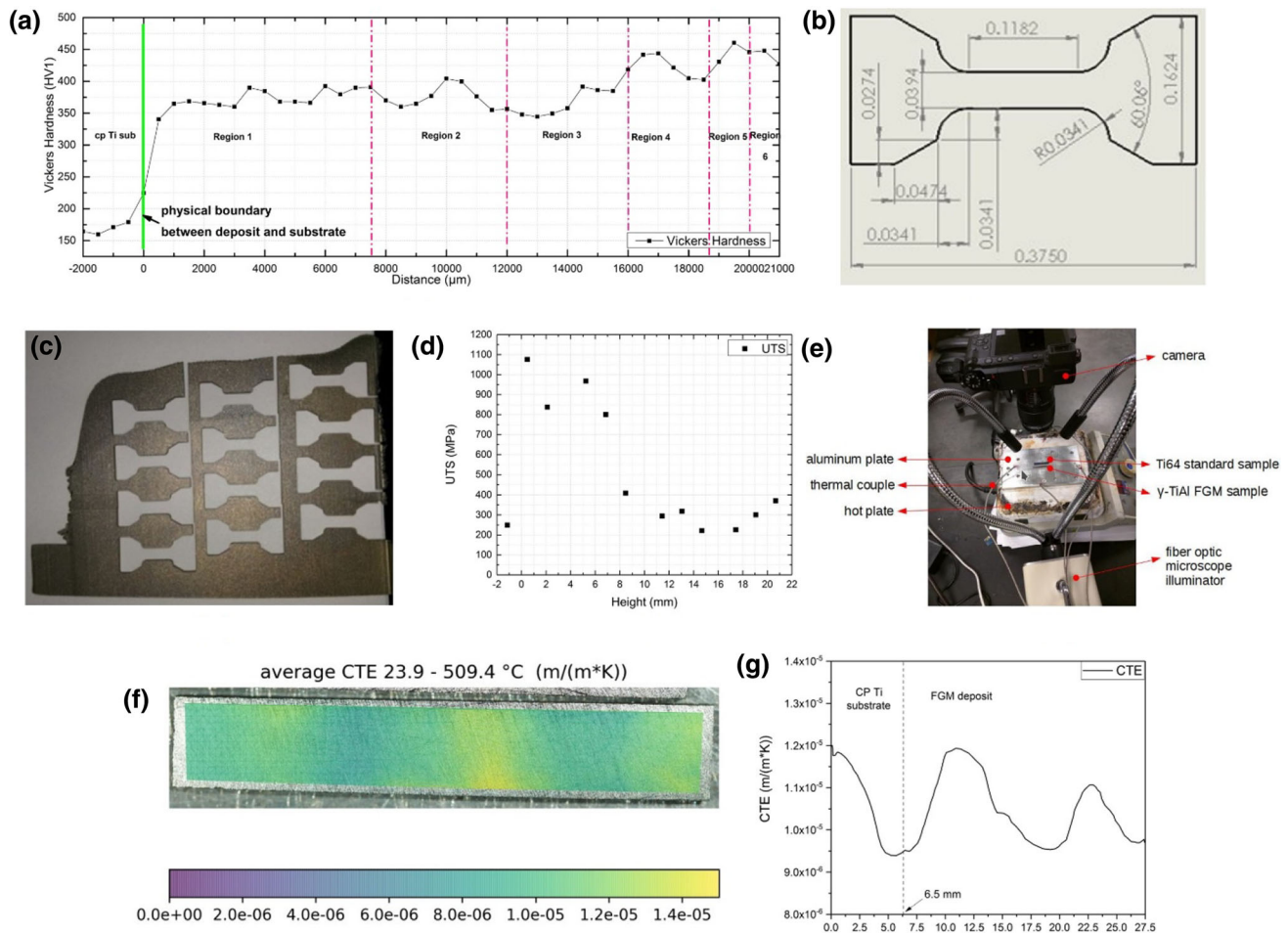


Fig. 4. Mechanical properties across the gradient alloy, (a) Vickers hardness test results, (b) test sample size, (c) dog bone layout, (d) UTS results, (e) CTE measurement set-up, (f) contour plot of average CTE values between 23.9–509.4°C, and (g) average CTE values along the gradient path between 23.9 and 509.4°C.

within 23.9–509.4°C along the gradient path are plotted in Fig. 4g. The DIC result shows that the CTE value is  $1.2\text{E}-5$  at the CP Ti side and  $1.0\text{E}-5$  at the TiAl side, showing a high accuracy compared to the cast  $\gamma$ -TiAl CTE value ( $1.08\text{E}-5$ ) reported in Ref. 28. The CTE value difference is a main reason that causes cracking during the bonding process of dissimilar materials. There is a less than 10% difference across the gradient path, which means the part fabricated from joining two dissimilar materials would have a good thermal mechanical property during multiple thermal cycles.

## CONCLUSION

To conclude, the current work extends the option to join a titanium alloy with  $\gamma$ -TiAl by demonstrating a gradient path fabricated with Ti and Ti4822 powder blends that cannot be achieved using standard metallurgy methods. Combined with EDS and XRD results, six regions were detected with primary phases  $\alpha$ ,  $\alpha_2$ , and  $\gamma$  within the gradient alloy. The Vickers hardness increased slightly as Ti4822 wt.%

increased in the regions and led to material brittleness, where elongation is less than 1% at tensile test. The DIC test revealed that across the gradient alloy, the difference in mean linear CTE ranging from 23.9°C to 509.4°C is around 10%. Future work will be focused on gradient composition section height optimization and Ti/TiAl FGM part ductility improvement.

## ACKNOWLEDGEMENT

This project was supported by The Boeing Co. through the Center for Aerospace Manufacturing Technologies (CAMT), National Science Foundation Grant No. CMMI-1547042, and the Intelligent Systems Center (ISC) at Missouri S&T. Their financial support is greatly appreciated.

## REFERENCES

1. M. Thomas and M.P. Bacos, *AerospaceLab* 3, 1 (2011).
2. J. Liu, M. Dahmen, V. Ventzke, N. Kashaev, and R. Poprawe, *Intermetallics* 40, 65 (2013).
3. H. Clemens and S. Mayer, *Adv. Eng. Mater.* 15, 191 (2013).
4. J. Liu, V. Ventzke, P. Staron, N. Schell, N. Kashaev, and N. Huber, *Adv. Eng. Mater.* 14, 923 (2012).

5. G.Q. Chen, B.G. Zhang, W. Liu, and J.C. Feng, *Intermetallics* 19, 1857 (2011).
6. W. Hofmeister and M. Griffith, *JOM* 53, 30 (2001).
7. V.K. Balla, M. Das, A. Mohammad, and A.M. Al-Ahmari, *Adv. Eng. Mater.* 18, 1208 (2016).
8. H.P. Qu and H.M. Wang, *Mater. Sci. Eng. A* 466, 187 (2007).
9. Y.B. Zhang, B.Y. Huang, and H.X. Li, *Adv. Mater. Res.* 306, 496 (2011).
10. W. Ge, F. Lin, and C. Guo, Functional gradient material of ti-6al-4v and  $\gamma$ -tial fabricated by electron beam selective melting. (utexas.edu, 2015). <http://sffsymposium.engr.utexas.edu/sites/default/files/2015/2015-48-Ge.pdf>. Accessed 15 Aug 2017.
11. F. Brueckner, A. Seidel, A. Straubel, R. Willner, C. Leyens, and E. Beyer, *J. Laser Appl.* 28, 022305 (2016).
12. L. Yan, W. Li, X. Chen, Y. Zhang, J. Newkirk, F. Liou, and D. Dietrich, *JOM* 69, 586 (2017).
13. O. Carvalho, M. Buciumeanu, S. Madeira, D. Soares, F.S. Silva, and G. Miranda, *Mater. Des.* 80, 163 (2015).
14. W. Li, S. Karnati, C. Kriewall, F. Liou, J. Newkirk, K.M.B. Taminger, and W.J. Seufzer, *Addit. Manuf.* 14, 95 (2017).
15. D.C. Hofmann, S. Roberts, R. Otis, J. Kolodziejska, R.P. Dillon, J.-O. Suh, A.A. Shapiro, Z.-K. Liu, and J.-P. Borgonia, *Sci. Rep.* (2014). doi:10.1038/srep05357.
16. R.V. Ramanujan, *Int. Mater. Rev.* 45, 217 (2000).
17. Y. Hao, R. Yang, Y. Cui, and D. Li, *Acta Mater.* 48, 1313 (2000).
18. Y. Liu, W. Xu, D. Xie, and Z. Li, *Mater. Res. Innov.* 18, S2-573 (2014).
19. S. Malinov, T. Novoselova, and W. Sha, *Mater. Sci. Eng. A* 386, 344 (2004).
20. S.M. Kelly and S.L. Kampe, *Metall. Mater. Trans. A* 35, 2004 (1861).
21. G. Yong, Z. Lijing, G. Wenli, and Z. Hu, *China Foundry (Engl. Ed.)* 8, 19 (2011).
22. R. Gupta, B. Pant, V. Agarwala, and P. Sinha, *Met. Sci. Heat Treat.* 55, 438 (2013).
23. L. Yan, X. Chen, W. Li, J. Newkirk, and F. Liou, *Rapid Prototyp. J.* 22, 810 (2016).
24. X. Chen, L. Yan, W. Li, F. Liou, and J. Newkirk, Effect of powder particle size on the fabrication of ti-6al-4v using direct laser metal deposition from elemental powder mixture. ([www.utexas.edu](http://www.utexas.edu), 2016). <https://sffsymposium.engr.utexas.edu/sites/default/files/2016/055-Chen.pdf>, Accessed 15 Aug 2017.
25. N. Shamsaei, A. Yadollahi, L. Bian, and S.M. Thompson, *Addit. Manuf.* 8, 12 (2015).
26. P. Peyre, P. Aubry, R. Fabbro, R. Neveu, and A. Longuet, *J. Phys. D Appl. Phys.* 41, 025403 (2008).
27. I.N. Maliutina, H. Si-Mohand, R. Piolet, F. Missemer, A.I. Popelyukh, N.S. Belousova, and P. Bertrand, *Metall. Mater. Trans. A* 47, 378 (2015).
28. P. Bartolotta, J. Barrett, T. Kelly, and R. Smashey, *JOM* 49, 48 (1997).
29. Y. Zhang, L. Yan, and F. Liou, *Opt. Lasers Eng.* (2017) (**In Press**).